Int. J. Electrochem. Sci., 13 **(2018)** 7157 – 7174, doi: 10.20964/2018.07.73

International Journal of ELECTROCHEMICAL SCIENCE
www.electrochemsci.org

Enhanced Corrosion Resistance of Anodic Films Containing Alumina Nanoparticles on as-rolled AZ31 alloy

Ying Long[1], *Liang Wu*[1,2,*], *Zhi Zhang*[1], *Andrej Atrens*[3], *Fu sheng Pan*[1,2,*], *Aitao Tang*[1,2], *Gen Zhang*[1]

[1] College of Materials Science and Engineering, Chongqing University, Chongqing 400044, China
[2] National Engineering Research Center for Magnesium Alloys, Chongqing University, Chongqing 400044, China
[3] School of Mechanical and Mining Engineering, The University of Queensland, Brisbane Qld 4072, Australia
[*]E-mail: wuliang@cqu.edu.cn

Received: 24 March 2018 / *Accepted:* 2 May 2018 / *Published:* 5 June 2018

In this work, the samples of magnesium alloy AZ31 were anodized in two kinds of electrolytes, each with and without alumina nanoparticles. The structure, morphology and composition of four kinds of films were characterized using X-ray diffraction (XRD), scanning electron microscopy (SEM) and energy dispersal spectroscopy (EDS), respectively. The corrosion behaviors of films were studied using electrochemical impedance spectroscopy and potentidynamic polarization curves. The wear behaviors were evaluated using a ball-on-disc rotating wear test. The results showed that the alumina nanoparticles tended to gather in cracks and pores leading to increased film density and lower corrosion rates. The wear rates of films were decreased by adding nanoparticles.

Keywords: composite anodic films, corrosion resistance,wear resistance, nanoparticles, magnesium alloy

1. INTRODUCTION

Magnesium alloys are the lightest of the metallic structural engineering materials. Their low density, high strength-to-weight ratio, good castability and good biocompatibility had led to increasing use in electronics, automotive, aeronautical and biomedical industries [1-6]. The versatility and moderate price [7] give magnesium alloys application potential. Nevertheless, two major drawbacks remain. Firstly, the low standard potential of magnesium provides a large driving force for corrosion, which is not countered by the corrosion product films. Impurities and second phases further increase the corrosion tendency. Secondly, there is wear so that magnesium alloys are applicable only in low-

intensity wear conditions [8]. Hence, finding ways to improve their resistance capacity to corrosion and wear is an imperative issue to promote applications of magnesium alloys [9-19].

Various methods have been studied to improve corrosion behavior including (i) increasing purity [20], (ii) optimizing casting processes [21] to eliminate segregation, to improve purity, and to form uniform microstructures, (iii) surface modification techniques such as anodic oxidization, electroplating [22], chemical conversion coatings [23] and physical vapor deposition coatings [24]. Meanwhile, to enhance wear resistance, (i) laser surface melting [25], (ii) ultrasonic impact treating [26], (iii) optimization of engineering design [27] have been developed to enhance wear performance.

Since corrosion and wear start at the surface, both properties may be improved by surface treatment such as anodizing [28], which can produce a relatively-thick, adherent hard oxide film on the substrate for surface protection [29]. However, corrosion protection may not be adequate because anodic films can be porous [30-32], so reducing porosity is a significant research topic.

Coating methods like plasma electrolytic oxidation are frequently used. Darband [33] studied plasma electrolytic oxidation of magnesium and its alloys. They found improvement in corrosion resistance, tribological properties and biological performance of surface coatings on magnesium. Yagi [34] found that plasma electrolytic oxidation (PEO) on ACM522 magnesium alloy in an aqueous silicate solution produced promising films. Although there were many nanocracks on the surface of the anodic oxide film, these cracks did not penetrate to the underlying substrate, which was consistent with Chai [35]. It shows the enhance of corrosion resistance by PEO technology. Above all, these studies have shown that PEO method can help improve corrosion resistance and wear resistance of anodic films to some degree. However, compared with anodizing, PEO layers have a relatively high porosity due to higher voltages and (normally) alternating currents that cause intense sparking and break down the oxide layer. For anodizing, low-voltage direct currents are used and the formation of the oxide layer occurs under a quiescent regime. The produced layer has relatively homogeneous structure [36]. Therefore, we choose to use anodizing to improve corrosion and wear resistance of anodic films on magnesium alloys.

Previous studies have shown that incorporating foreign particles into anodic oxide coatings is a promising method for controlling porosity [37]. Song [38] used an EIS model to study the corrosion of anodic films on AZ91D（8.3–9.7 wt.% Al, 0.35–1 wt.% Zn, 0.15–0.50 wt.% Mn), ZE41 (3.5–5 wt.% Zn, 0.4–1.0 wt.% Zr, 0.75–1.75 wt.% rare earth elements) and pure Mg (99.96 wt.%). They found that film defects caused substrate exposure to the electrolyte, and these areas corroded preferentially. Pores were the primary defects on anodic films, so decreasing porosity can restrict corrosion. A variety of particles (e.g. ZrO_2, TiO_2, CeO_2 and clay) have been successfully incorporated into plasma electrolytic oxide coatings [39-42] with some variation of film properties. Wang [43] added CeO_2 nanoparticles to produce Ni-Ti composite coatings. They found that the embedded CeO_2 nanoparticles facilitated the formation of a compact passive film on the surface of the composite coatings and helped to improve the corrosion resistance of the composite coatings. Turan [44] found that Magnesium/Graphene Nanoparticle (GNP) composites have negative effect for corrosion performance of magnesium. Wear resistance was enhanced with graphene content. Calderón J A [45] assessed erosion–corrosion resistance of Ni composite coatings with embedded SiC nanoparticles. They have noticed that the presence of inert particles of SiC in the conductive matrix coating may have blocked the passage of the

anodic current, diminishing the corrosion rate of the coating. The incorporation of SiC nanoparticles is responsible for increases in the microhardness of the composite coatings and a better resistance against erosion–corrosion.

In this work, anodic oxide films were fabricated in sodium silicate (Na_2SiO_3) electrolyte and sodium aluminate ($NaAlO_2$) electrolyte respectively. Alumina nanoparticles were added into the electrolyte to form composite anodic films. The effects of alumina nanoparticles and two electrolytes on the morphology and composition of anodic oxide films were studied using XRD, EDS and SFE-SEM. Potentidynamic polarization and EIS were used to evaluate corrosive behaviors of anodic oxide films. Ball-on-disc rotating wear test was used to measure wear performance. We have successfully confirmed the influence of alumina nanoparticles for preparing anodizing films on corrosion resistance and wear resistance of magnesium alloys.

2. EXPERIMENTAL

2.1. Materials

AZ31 magnesium alloy rolled sheet was cut into specimens of the following dimensions: 3 cm × 1.5 cm and 2.5 cm × 2.5 cm. Prior to the anodizing treatment, the surface of each specimen was ground on silicon carbide papers to a 1500 grit, cleaned with deionized water and ethanol separately, and dried in the air.

2.2. Procedures

Preparation of anodic oxide film: Anodizing was performed in a two-electrode cell, the as-rolled AZ31 sheet was the anode and stainless steel plate was the cathode. The current was supplied by a DC constant current power supply (WYJ-200V3A,China). The anodizing electrolyte was slowly stirred with a magnetic stirrer. Four anodizing processes were applied to produce four different anodic oxide films.

Firstly, for sample in $NaAlO_2$ anodizing electrolyte, anodizing was carried out at a voltage of 20 V for 20 minutes. The electrolyte contained 7.14g/L NaOH and 4g/L $NaAlO_2$ in distilled water.

The second group of samples was anodized in 5g/L NaOH, 25g/L Na_2SiO_3 electrolyte at 130 V for 20 minutes.

For the third group, 5g Al_2O_3 nanoparticles were added into the $NaAlO_2$ electrolyte to produce composite anodic films. Other anodizing parameters remain the same with the first group. Alumina nanoparticles used have a diameter of 40 nm and were purchased from Nanjing Emperor nano material Co., Ltd. Before anodic oxidation, alumina nanoparticles were treated by anionic surfactants (sodium dodecyl phosphate) and ultrasonic dispersion for 1 h.

For the last group, 5g Al_2O_3 nanoparticles were added into the Na_2SiO_3 electrolyte to produce composite anodic films. Other anodizing parameters remain the same with the second group. When the anodizing process was over, the samples were rinsed in deionized water and then dried in hot air.

2.3. Characterization

A field emission scanning electron microscope (FE-SEM, Nova 400 FEI, USA) was used to characterize the surface morphology and cross-sectional morphology of the coatings, operated at 10 kv. The elemental distribution in the anodic oxide film was examined using EDS (INCA Energy 350 Oxford, UK). Cross section samples were prepared by sampling machine and embedded in a room temperature curing epoxy resin, then ground and polished. The structure of the alloy and anodic films were investigated by XRD (D/Max 2500X Rigaku, Japan), using Cu Kα ray within 2θ. The data collection was performed with an incident beam length of 0.154056Å. The scanning range was 2θ from 5°to 80°. The scanning rate was 4°/min.

Electrochemical measurements were performed using an electrochemical workstation (CIMPS-2, Zahner, German) to measure polarization curves and electrochemical impedance spectra (EIS). A three-electrode system was used: a working electrode (the sample), a saturated calomel reference electrode (SCE) and a platinum plate counter electrode. All the electrochemical tests were carried out in a 3.5% NaCl solution. Polarization curves of all samples were obtained by switching the potential from −2 V in the cathodic direction to 0.5 V in the anodic direction. The reference to the open circuit potential is at a sweep rate of 2 mV/s.

Impedance measurements were swept at a 10 mV/rms sinusoidal perturbation. The tests performed at OCP from 10^{-2} to 10^{5}Hz. The experimental impedance plots were fitted employing different equivalent circuits by Zview software. All EIS tests and polarization were carried out at room temperature. To ensure the reproducibility, three parallel samples were used in each system.

2.4. Friction and wear test of oxide film

The wear test was carried out using a ball-on-disc rotating wear test machine (Huijintier, POD-1, China). The 304 stainless steel ball has a diameter of 5 mm and surface roughness of about 0.01 μm. The test was mainly rotary friction with a speed of 200 r/min. The load is 5 N. The wear mark has a diameter of 8 mm. The maximum friction force was 5 N. In each group, there were three parallel samples. Each parallel sample was tested for 1800s. All friction tests were conducted at room temperature. The surface morphology of the wear marks after the wear tests were examined by field emission scanning electron microscopy (FE-SEM, XL30S, FEI, USA). The composition of worn surfaces was analyzed by the EDS attached to the SEM. A Veeco Dektak 150 surface profile was applied to measure the depth profiles of wear tracks. And, making the area of wear mark multiplied by the oscillating amplitude can gain the wear volumes. All wear rates of the samples were calculated as

$$\omega = V/(L \times N) \quad (1)$$

ω is wear rate, V is wear volume, L is sliding distance, N is load.

3. RESULTS AND DISCUSSION

3.1. XRD analysis

Fig.1 shows XRD spectra of four as-rolled AZ31 samples anodized under different conditions. The XRD spectra of all samples have clear diffraction peaks. It can be seen that the height of (012) characteristic diffraction peak of crystal surface of four samples is different. (012) characteristic diffraction peak is located at about 35°. With the addition of alumina nanoparticles, the characteristic diffraction peak becomes sharp. This indicates that the completeness of crystal structure and the crystallinity of anodic films increase with the addition of alumina nanoparticles [46]. Furthermore, the characteristic diffraction peak at about 31° indicates alumina nanoparticles have successfully entered into anodic films of magnesium alloy. So the composite anodic films have been successfully fabricated on AZ31 samples.

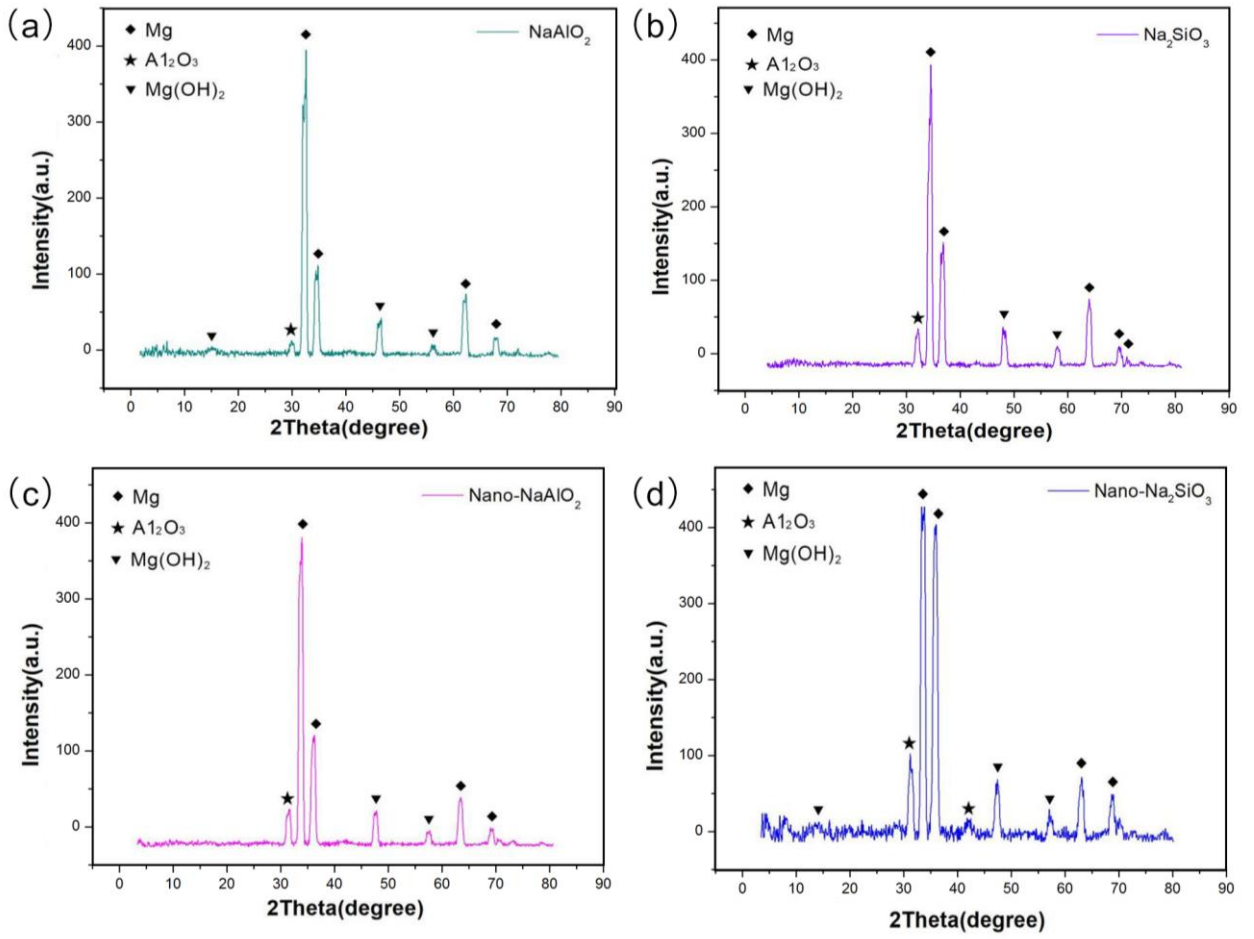

Figure 1. The XRD spectra of four anodic samples obtained in four different anodizing conditions: (a) fabricated in $NaAlO_2$ solution, (b) fabricated in Na_2SiO_3 solution, (c) fabricated in $NaAlO_2$ solution with nanoparticles, (d) fabricated in Na_2SiO_3 solution with nanoparticles. Peaks marked with ★ are caused by the alumina nanoparticles, ◆are caused by Mg phase and ▼ are caused by the $Mg(OH)_2$

3.2. SEM analysis

Fig.2 shows SEM images at lower and higher magnifications of the anodic oxide films on the AZ31 magnesium alloy. Fig.2b shows that the surface morphology of the anodic oxide film had a relatively rough, non-uniform, coarse surface covered by a great number of micro-scale bumps with irregularly shaped structures. When the anodizing started, the natural oxide film on AZ31 magnesium alloy substrate quickly dissolved.

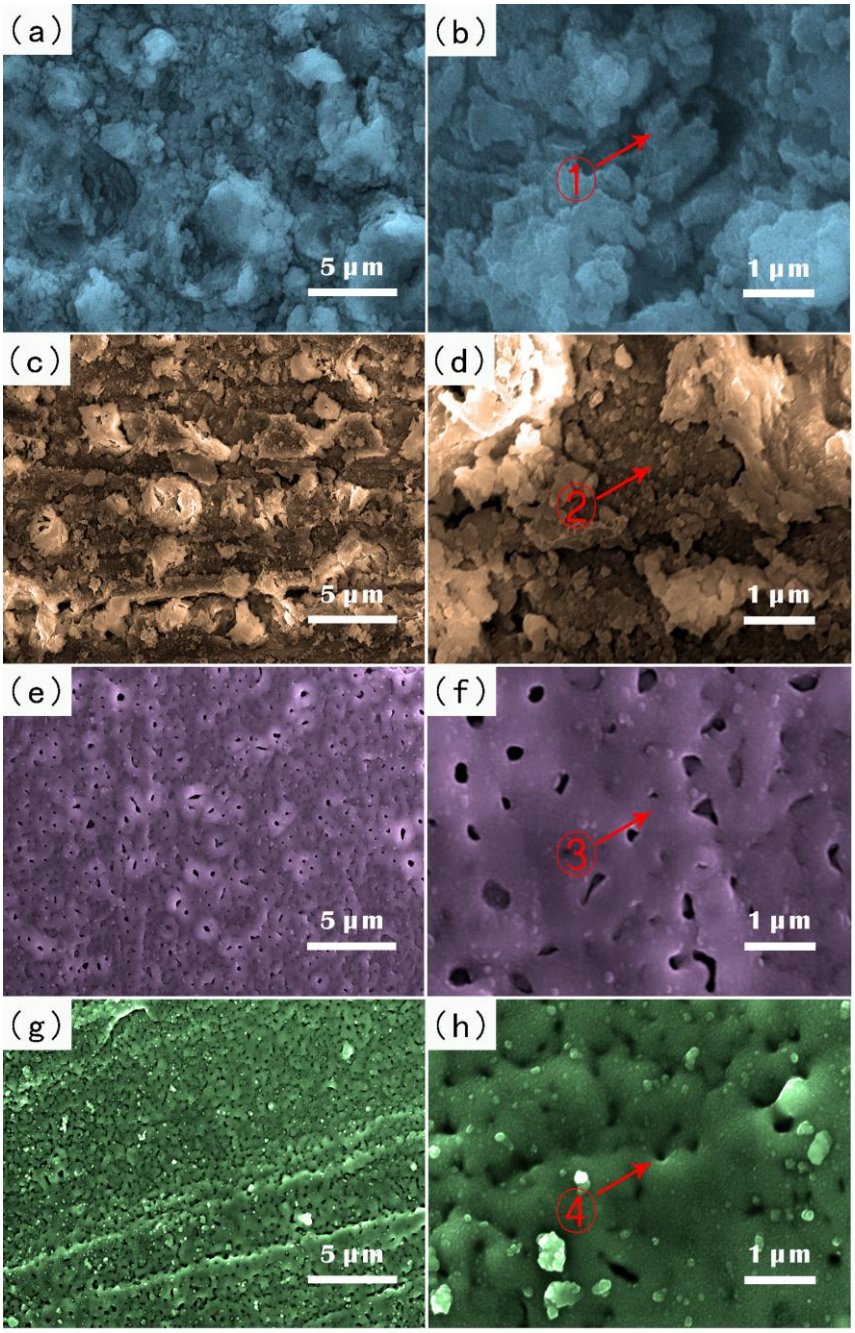

Figure 2. SEM images of four anodic samples obtained in four anodizing conditions with low and high power microscope: (a,b) fabricated in $NaAlO_2$ solution, (c,d) fabricated in $NaAlO_2$ solution with nanoparticles, (e,f) fabricated in Na_2SiO_3 solution, (g,h) fabricated in Na_2SiO_3 solution with nanoparticles

The magnified SEM images at higher magnification show that the rough structure of the anodic oxide film formed at the voltage of 20 V contains many nanocracks (Fig.2a,b), which were caused by internal stress [47]. The presence of cracks was detrimental to film corrosion resistance as the corrosive substance can penetrate to the magnesium substrate through the cracks [48]. The flake-shaped bumps were possible sites that support subsequent film growth. Fig.2f presents a dramatic variation of surface morphology with increasing anodization voltage to 130 V and switching electrolyte from $NaAlO_2$ to Na_2SiO_3. The perpendicularly grown film was more susceptible to dissolving under higher voltage, thus the film grows faster in the horizontal direction and does not form large bumps, resulting in a smoother coating with an ordered texture and smaller bumps [49]. The size of bump decreased, the film became relatively smooth with even distribution of pores (Fig.2e,f). The SEM images denote the difference of the anodizing condition (i.e. voltage and electrolytic bath) in the anodizing process and the influence on the morphology of anodized film. The regularity of the surface arrangement of the films was improved with increased applied voltage, which was in good agreement with previous work [12]. This can be attributed to the dissolving and regrowing of the anodized film at high voltage. However, excessively high current density often leads to a loose and porous anodic film [50-52] because furious sparking at high current density can result in the large size of chunks, pores and a higher degree of microcracks on the anodic film [53].

Fig.2f shows many disc-shaped nanobumps on the surface of the anodized film, which were considered to be the newly grown regions of the film. These bumps grew larger and covered the cracks. They gradually merged together, which enabled pores to form at the intersecting places. The structural change from nanocracks to nanopores can reduce film porosity, which led to less air trapped inside the surface layer, thus reduced alloy exposure to corrosive medium in the air.

Fig.2c indicates that both the number and size of bump on the surface increased remarkably compared with Fig.2a. This can be explained as follows: the attachment of the nanoparticles to the anodic film contributed to the increase of bumps. The resistance of the anodic oxide bath increased after the addition of nanoparticles, resulting in an increase in feedback voltage, which further accelerated the growth of some preferentially grown regions. This leads to large bump. Furthermore, while Fig.2e,g had comparable morphologies (the pores distributed uniformly), the pores on the film in Fig.2g were smaller in terms of size with alumina nanoparticles. This is attributed to the fact that nano particles can accelerate the growth of anodic oxide film. It causes the pores in the film to narrow. Meanwhile, some tiny bumps appear on the film in Fig.2h, but they were hard to detect because these bumps were equivalent in size with surrounding nanoparticles.

3.3. EDS analysis

Fig.3a-d and Table 1 show EDS data measured for anodic oxide films. The film mainly contained Mg and O with traces of Al and Na. F and Si increased the strength and ductility of magnesium [54-57]. F originated from sodium fluoride (NaF), which was incorporated into the film during anodic oxidation. Fig.3b,d illustrate the characteristics of anodized layers with nanoparticles. The peak intensities of Al increased, which agrees with the presence of alumina nanoparticles in the film. The peak intensities of Si and F were correspondingly decreased.

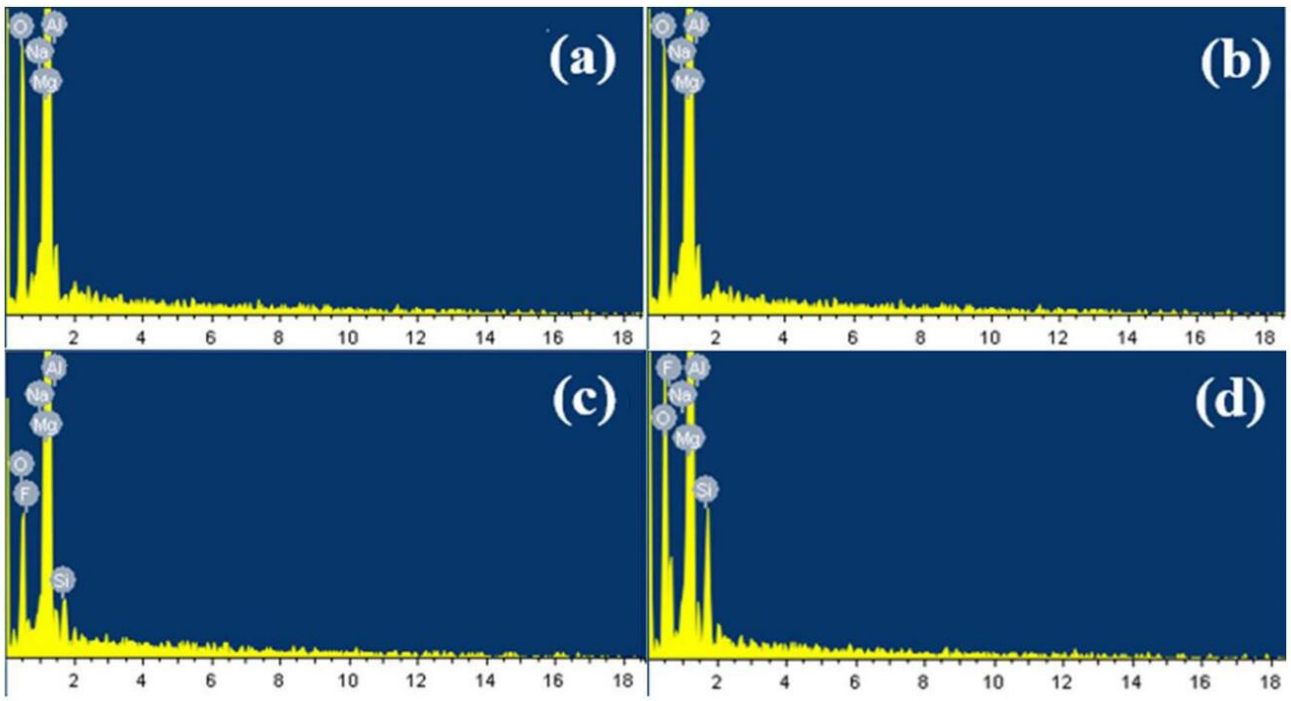

Figure 3. The EDS analysis of four anodic samples: (a) fabricated in $NaAlO_2$ solution, (b) fabricated in $NaAlO_2$ solution with nanoparticles, (c) fabricated in Na_2SiO_3 solution, (d) fabricated in Na_2SiO_3 solution with nanoparticles

Table 1. The EDS profile of four anodic samples

	$NaAlO_2$ solution	Na_2SiO_3 solution	$NaAlO_2$ solution with nanoparticles	Na_2SiO_3 solution with nanoparticles
O (at.%)	21.14	29.49	26.76	32.06
F (at.%)	—	9.67	—	2.51
N (at.%)	0.38	0.83	0.45	0.17
Mg (at.%)	76.64	54.53	70.52	76.56
Al (at.%)	1.84	1.35	2.27	1.59
Si (at.%)	—	4.13	—	2.10

3.4. Cross-sectional SEM analysis

Cross section morphology of anodized magnesium alloy after each anodizing treatment was observed. The lower layer is the AZ31 matrix. The anodic oxide layers had relatively non-uniform thickness in the range of 0.5-1.5 μm. Thicker films of approximately 1.5 μm was produced in the Na_2SiO_3 electrolyte, as shown in Fig.4c, because of the higher anodizing current density, which increased the growth rate and the thickness of the anodic oxide film [58]. With alumina nanoparticles, the thickness of the film slightly increased by 0.5 μm, as shown in Fig.4d. The density of anodic films increases, which agrees well with the SEM results in Fig.2. The film obtained under higher voltage

was also more dense and uniform, which is in accordance with the analysis of Fig.2 that high voltage condition is conducive to the formation of a smooth film [12].

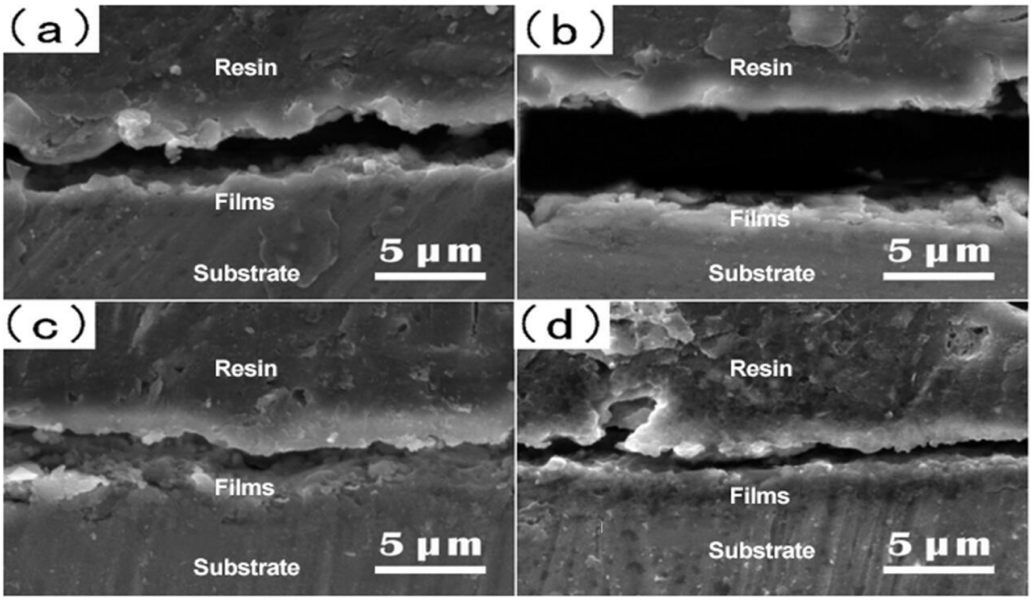

Figure 4. Cross-sectional morphology of four anodic samples: (a) fabricated in $NaAlO_2$ solution, (b) fabricated in $NaAlO_2$ solution with nanoparticles, (c) fabricated in Na_2SiO_3 solution, (d) fabricated in Na_2SiO_3 solution with nanoparticles

3.5 EIS analysis

Fig.5a,b present the Bode plots of the specimens in 3.5% NaCl solution. Assuming that the structure of the anodic film consisted of two layers [59], a dense inner layer and a loose outer layer [60], the impedance response at high-frequency was ascribed to the a loose outer layer, and the low frequency response was attributed to the inner compact layer [49]. Fig.5a indicates that in the high frequency range the phase angle was lower attributed to the penetration of the electrolyte due to the porous outer layer. The low frequency range contained a small loop can be seen due to the time constant of the barrier layer [61].

The impedance modulus values decreased for all samples, which may be related to the presence of aggressive F- ions that remained on the anodized film after anodizing, leading to the increase of corrosion rate. The impedance modulus (Z) at a frequency from 0.01 Hz to 100 Hz for sample $NaAlO_2$ was slightly lower than that for sample Na_2SiO_3, which means that the former has a lower barrier layer resistance. The impedance modulus value of sample Na_2SiO_3 with nanoparticles was higher than that of sample $NaAlO_2$ with nanoparticles and was the highest among all values, suggesting best sealing and protection performance.

Both samples with nanoparticles possessed higher impedance than that of samples without nanoparticles in all frequencies. Generally, a higher Z modulus at lower frequencies implies better corrosion resistance of the metal substrate [61-62]. Short times of anodizing (20 min) achieved high values of the impedance modulus (104–105 Ωcm^2) at low frequencies for samples with nanoparticles.

This result indicates the beneficial effect of nanoparticles on the corrosion resistance of the anodized magnesium film.

Table 2. Impedance parameters of four anodic samples obtained in four anodizing conditions (fabricated in $NaAlO_2$ solution, fabricated in Na_2SiO_3 solution, fabricated in $NaAlO_2$ solution with nanoparticles, fabricated in Na_2SiO_3 solution with nanoparticles) via the data of EIS fitted with the equivalent circuit

	$R_1/\Omega cm^2$	CPE_1-T $/\Omega cm^2$	CPE_1-P	R_2 $/\Omega cm^2$	CPE-T $/\Omega cm^2$	CPE_2-P	R_3 $/\Omega cm^2$	χ^2（E^{-3}）
$NaAlO_2$ solution	98.2	5.634E-6	0.504	3012	8.635E-9	0.827	1471	1.661
Na_2SiO_3 solution	106.1	1.104E-5	0.445	6002	6.038E-8	0.798	3203	1.843
$NaAlO_2$ solution with nanoparticles	267.2	5.854E-7	0.495	23257	5.051E-7	0.813	16224	0.832
Na_2SiO_3 solution with nanoparticles	298.5	1.754E-7	0.745	32205	5.832E-11	0.912	94420	0.738

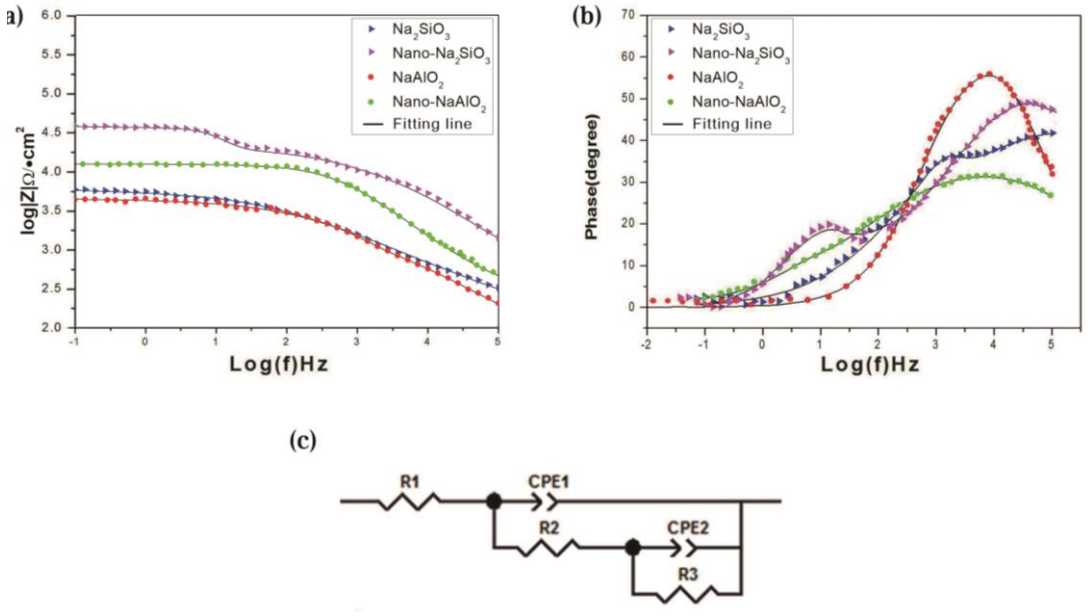

Figure 5. Bode Figure and the fit figure (a, b) of four anodic samples obtained in four anodizing conditions by being soaked in 3.5wt.% NaCl solution, (c) the equivalent circuit for the four samples

The equivalent circuit was used to fit the EIS data for different systems presented in Fig.5c. There were two time constants (CPE_1, R_2; CPE_2, R_3) and the resistance of electrolyte (R_1). R_2 represents the resistance of the porous sub-layer of the anodic oxide film. CPE_1 was the constant phase element of the outer layer, which depends on different factors such as film thickness and defect structure [63]. R_3, CPE_2 were assigned to the inner layer resistance and constant phase element respectively. The quality of fitting was evaluated by χ^2. Table 2 displays the results of simulation. R_3 of different samples reveal their differences in anti-corrosion performance [64].

Initially, the Na_2SiO_3 sample presented higher values of R_3 (3203/Ωcm^2) and R_2 (6002/Ωcm^2), compared with those of the $NaAlO_2$ sample, which decreased to 1471/Ωcm^2 and 3012/Ωcm^2 respectively. There were the same results after the addition of alumina nanoparticles. The increases of R_3 and R_2 were ascribed to less porosity of the anodic film, signifying stronger protective effect of Na_2SiO_3 sample. The fitting results indicate that R_3 and R_2 have an increase of one order of magnitude with alumina nanoparticles, implying the barrier properties of the anodic film were significantly improved via the addition of nanoparticles. The SEM image of the cross-section demonstrated no significant change in the thickness of the film. Combined with the SEM image of anodic oxide film, alumina nanoparticles improved the density of the film and reduced the size of holes. Moreover, with alumina nanoparticles, the anodic oxide film had a higher value of R_2. This indicated that the nano particles not only entered in the film but also anchored to the cracks and pores on the film, which gradually narrowed cracks and pores in anodizing. Hence, alumina nanoparticles effectively improved the corrosion resistance of the anodic oxide film on the magnesium alloy.

3.6 Potentidynamic polarization curve

Potentidynamic polarization curves were measured as presented in Fig.6. The corrosion potential (E_{corr}) and corrosion current density (I_{corr}) are presented in Table 3. The overall trend of the curves revealed that potential difference was widened by the progression of polarization. The current density has increased with potential shifting to active direction. The shapes of the curves were similar, but the corrosion potential was different (as shown in Table 3). This means that although corrosion behaviors of the anodic samples were similar, their corrosion resistance is different. Table 3 indicates that $NaAlO_2$ sample reached the lowest E_{corr} -1.2975V and the highest I_{corr} 6.31×10^{-6} A/cm^2 among all samples. In a typical polarization curve, a lower E_{corr} and higher I_{corr} corresponds to a lower corrosion rates [63,65]. Therefore, the $NaAlO_2$ sample has the poorest corrosion inhibition capacity, which can be ascribed to large quantities of cracks and pores on the surface. In contrast, for the Na_2SiO_3 sample, I_{corr} was lower by one order of magnitude, signifying an improvement of corrosion resistance consistent with the result of equivalent circuit simulation in Table 2. Meanwhile, for samples with nanoparticles, E_{corr} became higher and I_{corr} was lower, which shows an enhancement in corrosion resistance after the addition of alumina nanoparticles.

Table 3. The data of potentidynamic polarization curve results of four anodic samples. E_{corr}: the corrosion potential, I_{corr}: the corrosion current density

Sample	E_{corr} [V/SCE]	I_{corr} [A/cm^2]
$NaAlO_2$	-1.298	$6.31x10^{-6}$
$NaAlO_2$ solution with nanoparticles	-0.502	$1.78x10^{-6}$
Na_2SiO_3	-0.797	$8.89x10^{-7}$
Na_2SiO_3 solution with nanoparticles	-0.533	$3.16x10^{-7}$

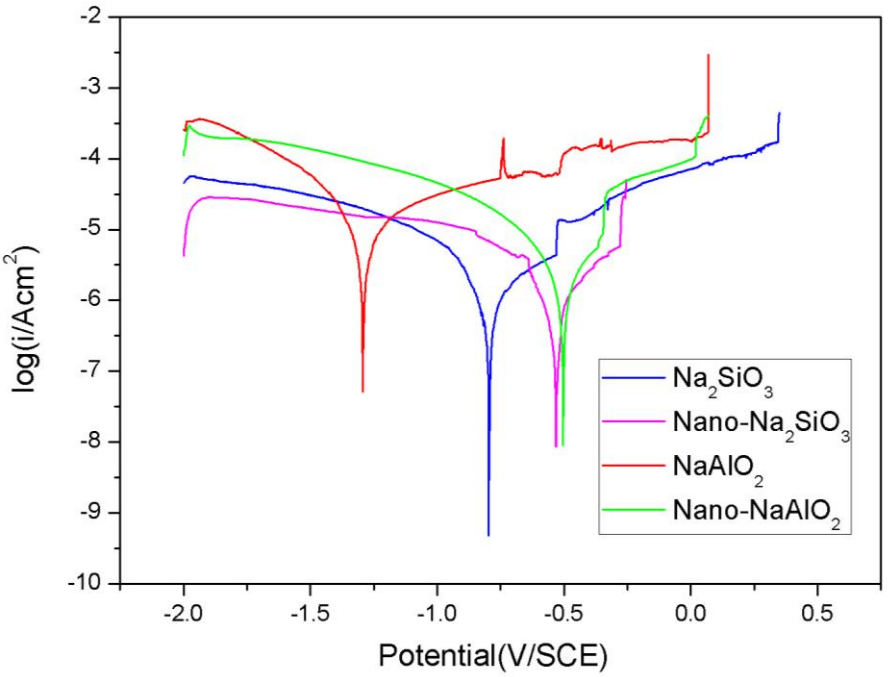

Figure 6. Potentidynamic polarization curves of four anodic samples obtained in four different anodizing conditions (fabricated in Na_2SiO_3 solution, fabricated in Na_2SiO_3 with nanoparticles, fabricated in $NaAlO_2$ solution, fabricated in $NaAlO_2$ solution with nanoparticles)

3.7 wear resistance analysis composite anodic films

Fig.7 reveals the variation of friction coefficient of four anodized samples and substrate vs time. This plot shows three regions associated with three regimes: friction first decreases, then increases and finally achieves a steady value at the rest of the sliding distance. In Fig.7, the change of the friction coefficient value is coupled with the evolution of the wear morphology [66]. The initial decline stopped at 200s. Then the friction coefficient started to increase. This can be explained as follows: after grinding for a period of time, wear marks deepened and the contact area with grinding

ball became larger, leading to the rise of friction coefficient. Fig.7 shows that the friction coefficient curve has relatively large fluctuation, which is likely to be caused by the rough surface of anodic oxide films and huge amount of debris particles [8]. With the prolongation of friction and wear time, the friction coefficient of the two samples with nanoparticles is lower than that of other samples, which can be interpreted as follows: the relatively high hardness of the nanoparticles enables the trend of rolling friction to form between nanoparticles and grinding balls. This reduced the friction coefficient.

Fig.8 shows the low and high magnification SEM images of four anodized samples after wear tests. There were strip-like wear marks on four samples. The higher magnification SEM images indicate a great many of debris distributed randomly at wear sites. The image of Na_2SiO_3 sample presents less debris, in comparison to $NaAlO_2$. For samples with nanoparticles, there were debris with relatively large size, which may be caused by the aggregation of alumina nanoparticles debris. EDS test analyzed the chemical composition of debris at wear sites in Fig.8. The results are presented in Table 4. Fig.8b,d indicate that the debris from samples without nanoparticles merely contained magnesium and oxygen, which were considered to come from few remnant fragments of the original magnesium oxide film. Aluminum was detected in debris from samples with nanoparticles, in Fig.8f,h. This indicated the presence of alumina nanoparticles in debris or the aluminum in the magnesium substrate.

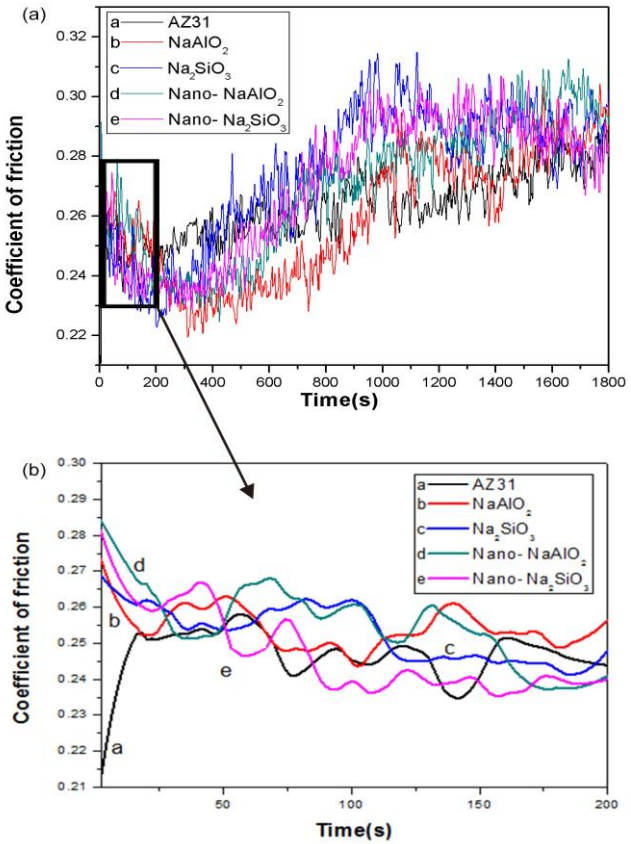

Figure 7. Friction coefficient - time curves of AZ31 magnesium substrate and four anodic samples obtained in four different anodizing conditions (fabricated in $NaAlO_2$ solution, fabricated in Na_2SiO_3 solution, fabricated in $NaAlO_2$ solution with nanoparticles, fabricated in Na_2SiO_3 solution with nanoparticles)

Fig.9 presents the depth and width of the wear marks of the four anodized samples measured by the step meter. Fig.10 shows the average wear rates of composite anodic films of four samples. The error bars represent the standard deviation. After calculation, the average wear rates of four anodic films fabricated in four different anodizing conditions are 5.2×10^{-5}, 4.375×10^{-5}, 3.3×10^{-5} and $2.5\times10^{-5}mm^3/(N\cdot m)$, respectively. That is to say, nanocomposite anodic oxide films with lower wear rates show better wear resistance. Meanwhile, the lost volume of four anodic oxide films after abrasion tests are about 27.5 mg, 20 mg, 18 mg and 10 mg respectively, decreasing monotonically. Sample Na_2SiO_3 with nanoparticles had the best wear resistance among four specimens, which was consistent with Fig.7. Anodic films with nanoparticles demonstrated better wear resistance, in which the wear volume of samples with nanoparticles had declined by half.

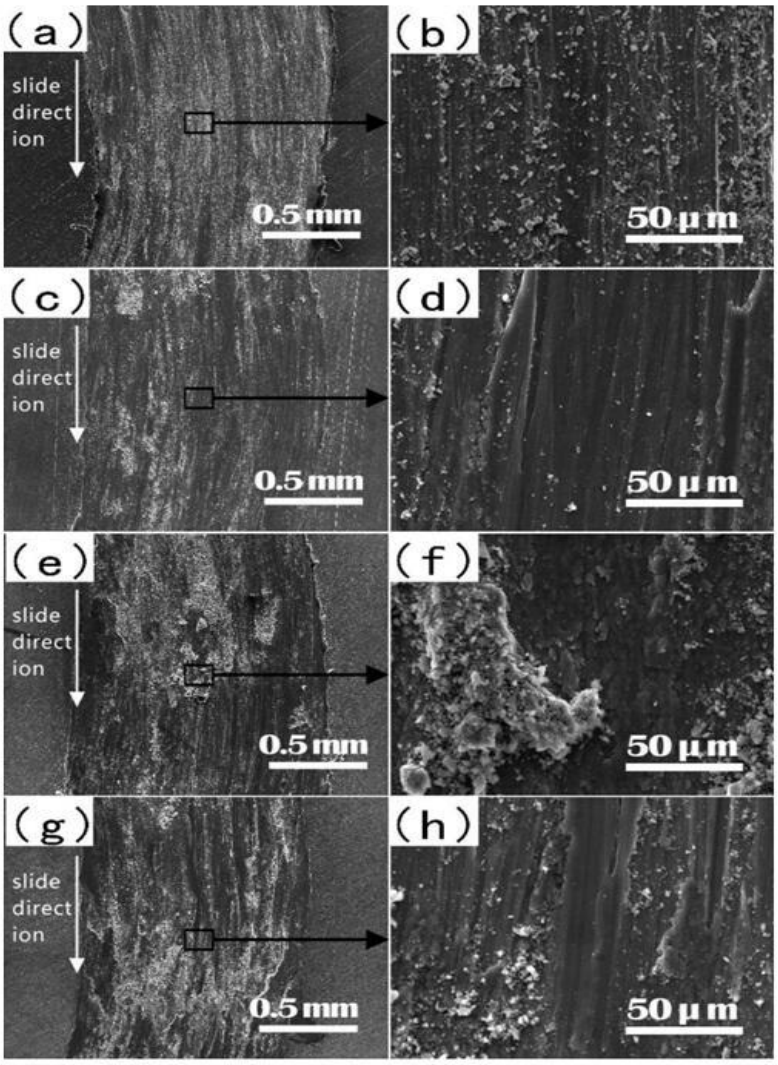

Figure 8. SEM images of four anodic samples: (a,b) fabricated in $NaAlO_2$ solution, (c,d) fabricated in $NaAlO_2$ solution with nanoparticles, (e,f) fabricated in Na_2SiO_3 solution, (g,h) fabricated in Na_2SiO_3 solution with nanoparticles

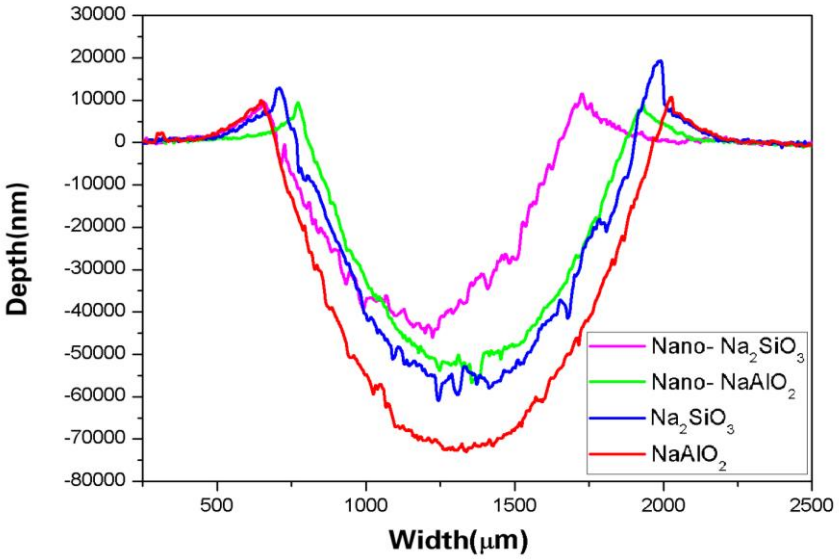

Figure 9. The width and depth of wear marks of four anodic samples obtained in four different anodizing conditions (fabricated in Na_2SiO_3 solution with nanoparticles, fabricated in $NaAlO_2$ solution with nanoparticles, fabricated in Na_2SiO_3 Solution, fabricated in $NaAlO_2$ solution)

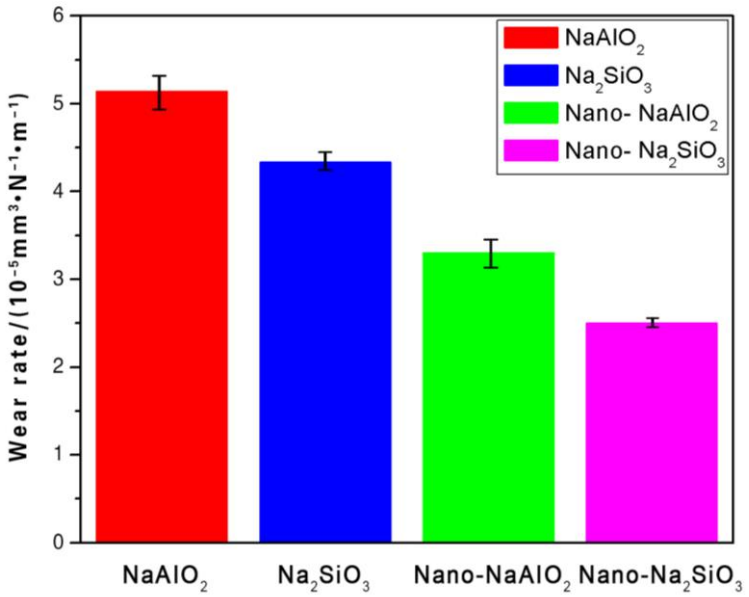

Figure 10. The volume of wear marks of four anodic samples obtained in four different anodizing conditions (fabricated in $NaAlO_2$ solution, fabricated in Na_2SiO_3 solution, fabricated in $NaAlO_2$ solution with nanoparticles, fabricated in Na_2SiO_3 solution with nanoparticles)

A reasonable explanation was that alumina nanoparticles turned sliding friction into rolling friction and reduced wear volume. Consequently, alumina nanoparticles could promote anti-wear and anti-friction performance of the composite anodic films, thus leading to an increase service time of magnesium alloy.

4. CONCLUSIONS

The effects of anodic oxidation of four different conditions on the morphology, anti-corrosive and anti-wear performance of anodic oxide film on AZ31 magnesium alloy were investigated. The following results were obtained:

1. Anodic oxide films have been successfully fabricated on AZ31 magnesium alloy via anodic oxidation. The morphology and chemical components of anodic oxide films were different due to the different anodizing electrolytes. The anodic oxide film of Na_2SiO_3 electrolyte was more compact and smooth compared with that in the $NaAlO_2$ electrolyte.

2. Corrosion resistance: samples fabricated in Na_2SiO_3 solution with nanoparticles >samples fabricated in $NaAlO_2$ solution with nanoparticles >samples fabricated in Na_2SiO_3 solution>samples fabricated in $NaAlO_2$ solution. Wear resistance: samples fabricated in Na_2SiO_3 solution with nanoparticles >samples fabricated in $NaAlO_2$ solution with nanoparticles >samples fabricated in Na_2SiO_3 solution >samples fabricated in $NaAlO_2$ solution.

3. Adding alumina nanoparticles into the electrolyte to fabricate composite anodic oxide films can improve corrosion resistance and wear resistance of AZ31 magnesium alloy.

ACKNOWLEDGEMENT
We acknowledge the financial support from the National Key Research and Development Program of China (2016YFB0301100),the National Natural Science Foundation of China (Project 51701029, 5153 1002, 51474043),the Student Research Training Program of Chongqing University (CQU-SRTP-2017153),the Chongqing Research Program of Basic Research and Frontier Technology (No. cstc2016 jcyjA0388), the Research and Development Project from COMAC and BOEING (2017-GT-088), China Postdoctoral Science Foundation Funded Project (2017M620410), the Chongqing Postdoc toral Scientific Research Foundation (Xm2017010).

References

1. G. Momen and M. Farzaneh, *Appl Surf Sci.*, 299 (2014) 41.
2. G. Zhang, L. Wu, A. Tang, S. Zhang, B. Yuan, Z. Zheng and F. Pan, *Adv. Mater. Interfaces*, 4 (2017) 1700163.
3. M. Q. Le, J. F. Capsal, M. Lallart, Y. Hebrard, A. V. D. Ham, N. Reffe, L. Geynet and P. J. Cottinet, *Prog. Aerosp. Sci.*, 79 (2015) 147.
4. L. Wu, G. Zhang, A. T. Tang, Y. L. Liu, A. Atrens and F. S. Pan, *J. Electrochem. Soc.*, 164 (2017) 339.
5. M. E. Turan, Y. Sun, Y. Akgul,Y. Turen and H. Ahlatci, *J. Alloy. Compd.*, 724 (2017) 14.
6. W. J. Joost and P. E. Krajewski, *Scripta. Mater.*, 128 (2016) 107.
7. S. You, Y. D. Huang, K. U. Kainer and N. Hort, *J. Magnes. Alloy*, 5 (2017) 239.
8. L. Wu, C. Wen, G. Zhang, J. H. Liu and K. Ma, *Vacuum*, 140 (2017) 176.
9. A. Němcová, O. Galal, P. Skeldon, I. Kuběna , M. Šmíd, E. Briand, I. Vickridg, J. J. Ganem and H. Habazaki, *Electrochim. Acta*, 219 (2016) 28.
10. M. Esmaily, J. E. Svensson, S. Fajardo, N. Birbilis, G.S. Frankel, S. Virtanen, R. Arrabal, S. Thomas, L. G. Johansson, *Prog Mater. Sci.*, 89 (2017) 92.
11. Y. Zhang, S. Tang, J. Hu and T. Lin, *Corros. Sci.*, 111 (2016) 334.

12. J. Wojciechowski, K. Szubert, R. Peipmann, M. Fritz, U. Schmidt, A. Bund and G. Lota, *Electrochim. Acta*, 220 (2016) 1.
13. R. Kondo, T. Kikuchi, S. Natsui and R. Suzuki, *Mater. Lett.*, 183 (2016) 285.
14. M. I. Ansari and D. S. G. Thakur, *Mater. Today*, 4 (2017) 9870.
15. G. Wu, W. Dai and H. Zheng, *Surf. Coat. Technol.*, 205 (2010) 2067.
16. W. Xu, J. Song, J. Sun, Y. Lu and Z. Yu, *Acs. Appl. Mater. Inter.*, 3 (2011) 4404.
17. A. Atrens, G. L. Song, M. Liu, Z. M. Shi, F.Y. Cao and M. S. Dargusch, *Adv. Funct. Mater.*,17 (2015) 400.
18. G. L. Song and A. Atrens, *Adv. Eng. Mater.*, 1 (1999) 11.
19. A. Atrens, G. L. Song, F. Cao, Z. Shi and P. K. Bowen, *J. Magnes. Alloy*, 1 (2013) 177.
20. R. E. McNultya and J. D. Hanawalta, *J. Electrochem. Soc.*, 81 (1942) 423.
21. Y. N. Doctor, D. B. T. Patil, A. M. Darekar, *Int. J. Ent. Sci.*, 6 (2013) 2319.
22. J. Y. Park, W. Se, S. Yoo and Y. H. Kim, *J. Alloy. Compd.*, 724 (2017) 492.
23. C. Wang, F. Jiang and F. Wang, *Corros. Sci.*, 46 (2004) 75.
24. R. A. Antunes and M. C. de Oliveira, Crit. *Rev. Biomed. Eng.*, 37 (2009) 425.
25. J. Z. Zhou, J. L. Xu, S. Huang, Z. R. Hu, X. K. Meng and X. Feng, *Surf. Coat. Technol.*, 309 (2016) 212.
26. H. B. Lin, Y. Y. Xia, X. S. Song and L. Z. Min, *Rare. Metal. Mat. Eng.*, 46 (2017) 17.
27. A. D. Waren, L. S. Lasdon and D. F. Suchman, *Proc. IEEE*, 55 (1967) 1885
28. P. B. Srinivasan, C. Blawert and W. Dietzel, *Mater. Sci. Eng. A*, 494 (2008) 401.
29. C. S. Wu, Z. Zhang, F. H. Cao, L. J. Zhang, J. Q. Zhang and C. N. Cao, *Appl. Surf. Sci.*, 253 (2007) 3893.
30. W. Y. Mu and Y. Han, *Surf. Coat.Technol.*, 202 (2008) 4278.
31. C. D. Gu, W. Yan, J. L. Zhang and J. P. Tu, *Corros. Sci.*, 106 (2016) 108.
32. G. L. Song and A. Atrens, *Adv. Eng. Mater.*, 5 (2003) 837.
33. G. B. Darband, M. Aliofkhazraei, P. Hamghalam and N. Valizade, *J. Magnes. Alloy*, 5 (2017) 74.
34. S. Yagi, K. Kuwabara, Y. Fukuta, K. Kubota and E. Matsubara, *Corros. Sci.*, 73 (2013) 188.
35. L. Chai, X. Yu, Z. Yang, Y. Wang and M Okido, *Corros. Sci.*, 50 (2008) 3274.
36. A. Lugovskoy and M. Zinigrad, *Materials Science - Advanced Topics*, InTech, (2013) Janeza Trdine 9, 51000 Rijeka, Croatia.
37. R. Arrabal, E. Matykina, P. Skeldon and G. E. Thompson, *J. Mater. Sci.*, 43 (2008) 1532.
38. G. L. Song and Z. Shi, *Corros. Sci.*, 85 (2014) 126.
39. S. Gowtham, S. Hariprasad, T. Arunnellaiappan and N. Rameshbabu, *Surf. Coat.Technol.*, 313 (2017) 263.
40. C. H. Sheyla, J. Gutierrez, and A. Tercjak, *Eur. Polym. J.* , 94 (2017) 87.
41. L. T. Seop, H. S. Ryu and S. H. Hong, *Corros. Sci.*, 62 (2012) 104.
42. G. Rapheal, S. Kumar, N. Scharnagl and C. Blawert, *Surf. Coat.Technol.*, 289 (2016) 150.
43. L. B. Wang, M. Chen, H. B. Liu, C. H. Jiang, V. Ji and F. M. Wang, *Surf. Coat.Technol.*, 331 (2017) 196.
44. M. E. Turan, Y. Sun, Y. Akgul, Y. Turen and H. Ahlatci, *J. Alloy. Compd.*,724 (2017) 14.
45. J. A. Calderón, J. E. Henao and M. A. Gómez, *Electrochim. Acta.*, 124 (2014) 190.
46. L. Wu, Z. C. Zheng, F. S. Pan, A. T. Tang, G. Zhang and L. Liu, *Int. J. Electrochem. Sc.*,12 (2017) 6352.
47. Q. V. Overmeere, F. Blaffart and J. Proost, *Electrochem. Commun.*, 12 (2010) 1174.
48. A. Manavbasi, S. Nibhanupudi, K. Bodily, T. Clarke, K. Johnson and B. Estes,*T. I. Met. Finish.*, 110(2012)17.
49. L. Wu,D. N. Yang, G. Zhang, Z. Zhang, S. Zhang, A. T. Tang, F. S. Pan, *Appl. Surf. Sci.*, 431 (2017) 177.
50. S. Verdier, M. Boinet, S. Maximovitch, and F. Dalard, *Corros. Sci.*, 47 (2005) 1429.
51. Y. Zhang ,Y. Wu and D. Chen, *Surf. Coat.Technol.*, 321 (2017) 236.

52. K. Tatsuya, N. Daiki, N. Osamu, N. Shungo and S. R. O, *Curr. Nanosci.*, 11 (2015) 560.
53. M. Mohedano, M. Serdechnova and M. Starykevich, *Mater. Design*, 120 (2017) 36.
54. N. Xiang, R. G. Song, J. J. Zhuang, R. X. Song, X. Y. Lu and X. P. Su, *T. Nonferr. Metal. Soc.*, 26 (2016) 806.
55. J. Wang, R. D. Liu, T. J. Luo and Y. S. Yang, *Mater. Design*, 47 (2013) 746.
56. K. Elangovan, C. S. Narayanan and R. Narayanasamy, *Comp. Mater. Sci.*, 47 (2010) 1072.
57. K. Velmanirajana, K. Anuradhab, A. S. A. Thaheerc, R. Narayanasamyd, R. Madhavane and S. Suwas, *Arch. Civ. Mech. Eng.*, 14 (2014) 398.
58. R. H. U. Khan, A. Yerokhin, X. Li, H. Dong and A. Matthews, *Surf. Coat.Technol.*, 205 (2010) 1679.
59. Z. Yao, Y. Xu, Z. Jiang and F. Wan, *J. Alloy. Compd.*, 488 (2009) 273.
60. J. Tedim, A. C. Bastos, S. Kallip, M. L. Zheludkevich and M. G. S. Ferreira, *Electrochim. Acta*, 210 (2016) 215.
61. M.Iannuzzi, T. Young and G. S. Frankel, *J. Electrochem. Soc.*, 153 (2006) B533.
62. X. Lu, C. Blawert, K. U. Kainer and M. L. Zheludkevich, *Electrochim. Acta*, 196 (2016) 680.
63. X. X. Guo, S. L. Xu,, L. L. Zhao, W. Lu, F. Z. Zhang, D. G. Evans and X. Duan, *Langmuir*, 25 (2009) 9894.
64. J. Wang, D. D. Li, Q. Liu, X. Yin, Y. Zhang, X. Y. Jing and M. L. Zhang, *Electrochim. Acta*, 55 (2010) 6897.
65. S. L. Zheng, C. Li, Q. T. Fu, M. Li, W. Hu, Q. Wang, M. P. Du, X. C. Liu and Z. Chen, *Surf. Coat.Technol.*, 276 (2015) 341.
66. M. Guezmil, W. Bensalah, A. Khalladi, K. Elleuch, M. D. Wery and H. F. Ayedi, *T . Nonferr. Metal.Soc.*, 25 (2015) 1950.